

# Vibration energy harvesting based on stress-induced polarization switching: a phase field approach

Dan Wang<sup>1,2</sup>, Linxiang Wang<sup>1</sup> and Roderick Melnik<sup>2</sup>

<sup>1</sup> State Key Laboratory of Fluid Power and Mechatronics Systems, Zhejiang University, 310027 Hangzhou, People's Republic of China

<sup>2</sup> MS2Discovery Interdisciplinary Research Institute, Wilfrid Laurier University, Waterloo, ON N2L 3L5, Canada

E-mail: [wanglx236@zju.edu.cn](mailto:wanglx236@zju.edu.cn)

Received 24 November 2016, revised 3 April 2017

Accepted for publication 20 April 2017

Published 16 May 2017



CrossMark

## Abstract

Different from the traditional piezoelectric vibration energy harvesting, a new strategy based on stress-induced polarization switching has been proposed in the current paper. Two related prototypes are presented and the associated advantages and drawbacks have been discussed in detail. It has been demonstrated that, with the assistance of a bias electric field, the robustness of the energy harvesters is improved. Furthermore, the real-space phase-field model has been employed to study the nonlinear hysteretic behavior involved in the proposed energy harvesting process. A substantially larger electric current associated with the stress-induced polarization switching has been demonstrated when compared with that with piezoelectric effect. In addition, the effects of bias electric potential, bias resistance, mechanical boundary conditions, charge leakage and electrodes arrangements have also been investigated by the phase-field simulation, which provides a guidance for future real implementations.

Keywords: vibration energy harvesting, ferroelectrics, polarization switching, phase field

(Some figures may appear in colour only in the online journal)

## Introduction

With continuous achievements in semiconductor manufacturing and MEMS/NEMS technologies, functionality of small electronic devices has been largely broadened and the electrical power consumption has been decreased to sub-milliwatt level. However, in some applications, such as wireless sensor networks and implantable biomedical devices, replacement of batteries at the end of their service life can still be costly or even impractical. In the last two decades, vibration energy harvesting has emerged as a promising solution for such challenges [1–3]. Various strategies have been proposed to convert mechanical energy from vibration into electrical power, including electrostatic induction, electromagnetic induction, piezomagnetic effect and piezoelectric effect. Among all the strategies, vibration energy

harvesting via piezoelectric/ferroelectric materials has been most widely and intensively investigated for its high energy density and high flexibility of being integrated with the MEMS/NEMS technologies.

Most investigations of the vibration energy harvesting via piezoelectric/ferroelectric materials in the literature to date are confined to the linear piezoelectric effect. To generate sufficient energy density, the energy harvesting device must perform at its resonant frequency. As the main frequency components of the vibration sources accessible are limited to the low frequency range, much of the current research focuses on lowering the resonant frequency of the energy harvesting structures [4–6]. Another current research focus is to broaden the resonant frequency range by introducing nonlinear effects into the structure [7–9]. With the improvement in material synthesizing technologies, vibration energy harvesting via

single crystal ferroelectrics, which have a supreme piezoelectric coefficient over ferroelectric ceramics, has also been investigated by several researchers [10, 11].

In addition to the linear piezoelectric effect used in conventional vibration energy harvesting, several new strategies have been proposed to harvest mechanical energy via ferroelectric materials in recent years. In [12, 13], a novel approach was demonstrated by Lynch *et al* to harvest mechanical energy by taking advantage of a stress-induced phase transformation in [011] cut PIN-PMN-PT single crystals. During the ferroelectric rhombohedral to ferroelectric orthorhombic phase transformation, an abrupt polarization change was induced which is significantly greater than that during the linear piezoelectric process. With appropriate electrodes arrangement, the polarization change resulted in a dramatic electric current which could be used or stored in the energy harvesting circuit. The influence of frequency and load resistance on the energy harvesting performance was also discussed. An increase by tens to hundreds times of harvested energy was demonstrated compared to that harvested with the same crystals operating in the linear piezoelectric regime. In [14, 15], Vaish *et al* presented a new technique for giant mechanical energy harvesting by mimicking the famous Olsen cycle which was proposed by R B Olsen in the early 1980s for enhanced thermal-electrical energy harvesting. The corresponding mechanical-electrical cycle was consisted of two isostress and two isoelectric field processes. The mechanism behind the cycle was ascribed to the ferroelectric/antiferroelectric transformation which is similar to that used in the explosive driven ferroelectric generator. The theoretical calculation results showed that the harvesting energy density could be several orders of magnitude larger than the highest energy density by linear piezoelectric effect reported in the literature. These two new strategies demonstrate considerable advantages in energy density over the traditional piezoelectric energy harvesters. However, both of them are limited in using ferroelectric bulk materials and rely on the effect of stress-induced phase transformation.

Based on a phase-field investigation of the stability of several nanoscale periodic domain patterns, a conceptual design of a thin film vibration energy harvester has recently been proposed by Huber *et al* [16]. A periodic stripe-type domain pattern was employed in their work. By bending the substrate, 90° ferroelastic domain wall was forced to sweep back and forth, causing a macroscopic electric charge change on the film surface. During the working cycle, the volume of different domains accommodated according to the external stress level, whereas the topology of the domain pattern remained unchanged. The concept is very interesting and attractive for its theoretically large energy density compared to that using piezoelectric effect. However, the application of this concept largely relies on the stability of the domain pattern. As is well known, the stability of the domain configuration is very sensitive to many factors, such as the size, the boundary conditions of the devices and the impurities or defects distribution in the materials [17–19]. So the robustness of this concept is deficient and needs to be carefully re-examined.

Inspired by the work reviewed above, a new strategy is presented in this paper. Similar to the work in [16], the mechanism is based on the stress-induced polarization switching. To get a high electric current output, a significant polarization change associated with external stress is always pursued. The polarization change in linear piezoelectric effect can be regarded as an intrinsic component which is due to stress dependence of the spontaneous polarization magnitude within ferroelectric domains. In addition to the intrinsic contribution, the whole polarization can also be changed due to the extrinsic contribution during the change of domain structures which can be altered by external stress (stress-induced polarization switching). There is an overwhelming superiority in magnitude for the extrinsic contribution compared with the intrinsic one. So it is reasonable to expect that the energy density will be largely increased, which has been theoretically proved in [16]. Here, instead of relying on the stability of the domain pattern, a bias electric field is imposed to ensure a stable repeatable working cycle. With the prescribed mechanism, two novel energy harvesting prototypes are proposed. Like in the traditional piezoelectric energy harvesting device, a ferroelectric film is deposited on a cantilever type structure. Different electrode modes (parallel plate mode and interdigitated mode) are manufactured on the thin film which can be used to apply a bias electric field and be connected to the harvesting circuit. The stress-induced polarization switching causes a reversible polarization change along the electrodes direction which is represented by the AC current in the harvesting circuit. Working process is slightly different in the two proposed prototypes. In what follows, advantages and drawbacks associated with them are addressed in detail. Furthermore, the analysis of processes and phenomena in the prototypes is carried out by the state-of-the-art real-space phase field model, and the effects of bias electric potential, bias resistance, mechanical boundary conditions, charge leakage and electrodes arrangements are carefully studied and discussed. The phase field simulation demonstrates possible advantages and drawbacks of the proposed strategy and provides useful instructions for future real implementations.

## Methods

### *Stress-induced polarization switching*

Ferroelectric materials are a subgroup of piezoelectric materials and are distinguished from the others for their spontaneous polarizations which can be switched by external electric field or stress under Curie temperature. The phenomena and underlying mechanism for polarization switching in ferroelectrics have already been demonstrated and well addressed in the literature. In addition, the mechanism has been used by several researchers for invoking novel MEMS actuators [20, 21]. Here, we only briefly introduce stress-induced polarization switching phenomenon, and for more details, [22, 23] can be consulted. As shown in figure 1, when ferroelectric materials are exposed to an external stress which

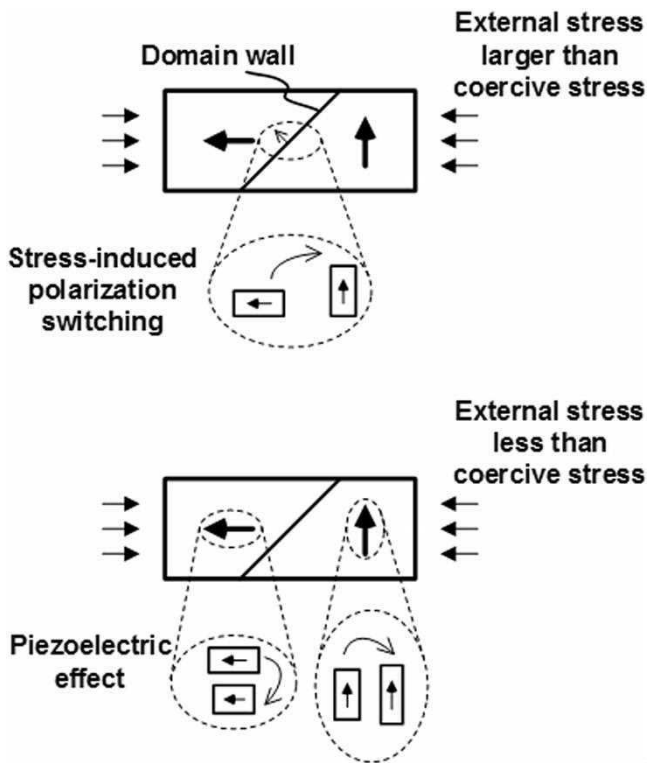


**Figure 1.** Comparison of stress-induced polarization switching and piezoelectric effect.

is larger than the coercive stress, polarization switching will be induced. The polarization switching takes place mainly via non  $180^\circ$  domain wall motion. In addition to the domain wall motion, domain wall nucleation and collapse can also be induced, which makes it difficult to keep the topology of the domain pattern unchanged. When the external stress is less than the coercive stress, no stress-induced polarization switching will happen. But the external stress will cause a change in spontaneous polarization according to the piezoelectric effect. To get a macroscopic piezoelectric polarization change, the ferroelectric materials must be poled first. The polarization change associated with stress-induced polarization switching is orders of magnitude larger than that with the piezoelectric effect. The associated process is intrinsically nonlinear and hysteretic and requires to be carefully treated.

#### *New vibration energy harvesting prototypes*

To convert the huge polarization change in stress-induced polarization switching process into useful electrical energy, two new vibration energy harvesting prototypes are proposed. For the first prototype, similar to the traditional vibration energy harvesting devices, a ferroelectric thin film is deposited on a vibration structure, such as a cantilever. The vibration of the structure leads to stretching or compression of the thin film, which is confined in the linear piezoelectric region in traditional harvesting devices, but here it must be larger than the coercive stress to induce polarization switching. On both sides of the thin film are electrodes which are connected to the harvesting circuit. As

shown in figure 2, when subjected to compressive stress, the initially horizontal polarization will try to switch vertically (Tetragonal symmetry is assumed here for simplicity). However, according to the symmetry involved, two possible variants (upward and downward) could be induced with equal chance. To get a macroscopic polarization change along the electrodes direction (vertical direction), a preference must be introduced. Thus a constant downward external electric field is applied by connecting the electrodes to a DC voltage source. In addition, to sense or capture the vibration-induced electrical energy, a resistance is connected with the DC voltage source in series. The simple energy harvesting circuit taken here is shown in figure 2(b). It is similar to that taken by Ullakko *et al* in their work for mechanical energy harvesting via magnetic shape memory alloy [24]. It needs to be pointed out that in a complete energy harvesting cycle, ideally, no energy is extracted from the DC voltage source. The work done by the DC voltage source can be calculated by:

$$W_{DC} = \int U_{DC} Idt = U_{DC} \int Idt = U_{DC} (Q_{out} - Q_{in}), \quad (1)$$

where  $Q_{out} - Q_{in} = 0$  holds in a complete cycle. Additionally, the mechanical work done by external stress is converted into two parts. One part is dissipated into thermal energy during the microstructure evolution process and the other part is converted to useful electrical energy via electric-elastic coupling effect, which is harvested by the bias resistance at last. A potential drawback associated with the first prototype is that a tensile stress must be applied to switch back the vertical downward polarization. However, most of the commercially available ferroelectric ceramics are very sensitive to such tensile stress. Ferroelectric single crystals may provide a possible solution for their excellent mechanical properties.

Another prototype is illustrated in figure 3, where interdigitated electrodes are used instead of parallel plate ones. In the initial state without external compressive stress, the polarization distribution is determined by the bias electric field. When a large enough compressive stress is applied, stress-induced polarization switching takes place. The stress-unfavored horizontal polarization will try to switch vertically, which leads to a macroscopic polarization reduction along the external electrodes direction (horizontal direction). In this case, both types of the vertical polarization variants can be induced as no external preference is imposed in the vertical direction. However, it will not affect the performance of the devices for only polarization along the electrodes direction that matters. When the compressive stress is withdrawn, the vertical polarization will automatically switch back under the influence of the bias field. So no tensile stress is needed. Here, the role of the bias electric field, which gives both preference (along electrodes direction) and backward switching force, is slightly different from that in the former prototype. Theoretically, the bias electric field strength here should be larger than that in the parallel plate prototype. Conclusively, the effect of the external stress in this prototype can be regarded as depolarizing the polarization along the bias electric field

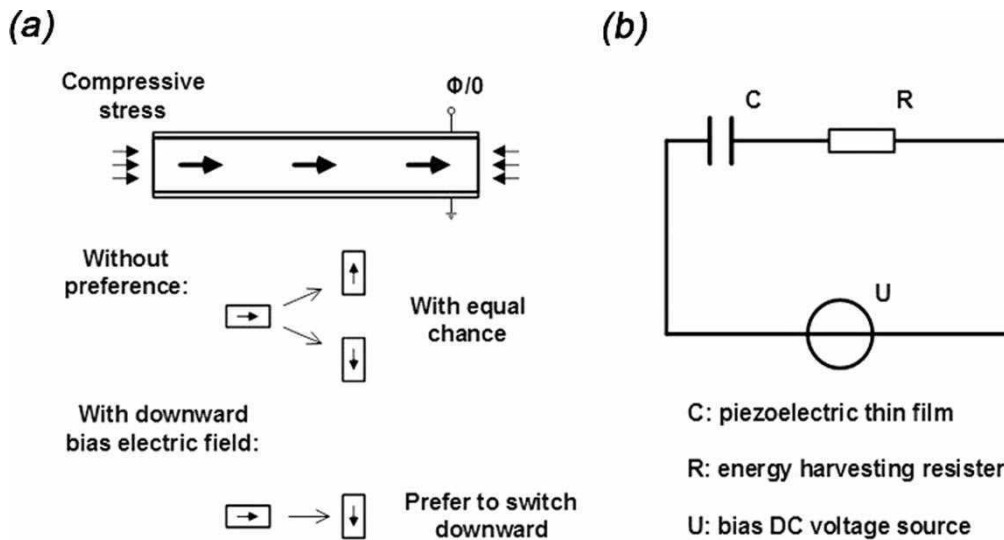


**Figure 2.** Demonstration of the prototype with parallel plate electrodes: (a) working mechanism; (b) energy harvesting circuit.

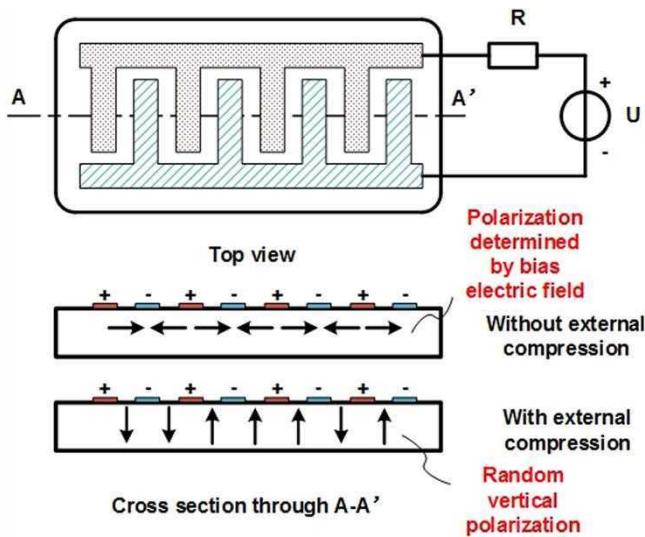


**Figure 3.** Demonstration of the prototype with interdigitated electrodes.

direction through stress-induced polarization switching. Similar mechanism has been investigated by Carman *et al* for vibration energy dissipation [25].

With the above strategy, the energy density is largely increased when compared to the traditional linear piezoelectric harvester. Furthermore, the robustness deficiency problem associated with the work in [16] is also improved. Theoretically, the application of the proposed strategy is no more confined to the nanoscale single crystal situation. It can even be applied in the macroscale range with ferroelectric ceramics, only if the stress-induced polarization switching is induced. However, as pointed out above, the process related to the stress-induced polarization switching is intrinsically nonlinear and hysteretic and requires further analysis. The state-of-the-art phase field model is implemented in the following sections to investigate the working process. Additionally, several important factors, which have pronounced

impacts on the energy harvesting performance, are carefully discussed.

### Phase field model and numerical implementation

In the last two decades, phase field models based on Ginzburg–Landau theory have emerged as a powerful tool to investigate microstructures in ferroelectric, ferromagnetic and multiferroic materials [16–19, 26, 27]. A lot of works by various researchers have been devoted to phase field modeling of phase and domain structures and their evolution in ferroelectric materials. In addition, the phase field model approach has recently been extended to real-space simulation, which enables us to address any ferroelectric structures with arbitrary geometries and boundary conditions [28–31]. As in [16], the state-of-the-art real-space phase field model is used in the current paper to investigate the nonlinear hysteretic behavior involved in the energy harvesting process. The model established by Bhattacharya *et al* in [28] is employed and the associated model parameters are adopted (BaTiO<sub>3</sub> was considered in their simulations). The governing equations are normalized following the same procedure as presented in the paper mentioned. Details regarding the model and material parameters are presented in the appendix. For further information, [28] can be consulted.

The model is numerically implemented with the general PDE module in COMSOL Multiphysics, where the finite element method with backward differentiation is applied. For simplicity, only a two-dimensional simulation is carried out. The computational area and boundary conditions are shown in figure 4. A rectangle with normalized dimension  $1600 \times 200$  ( $l' \times h'$ ) is considered. The middle element on the lower boundary is simply supported. A shear force with the distribution shown in the figure is applied on the lower boundary, which resembles the stress distribution imposed by the deformed substrate. The maximum magnitude of the shear force changes with time following the sine law

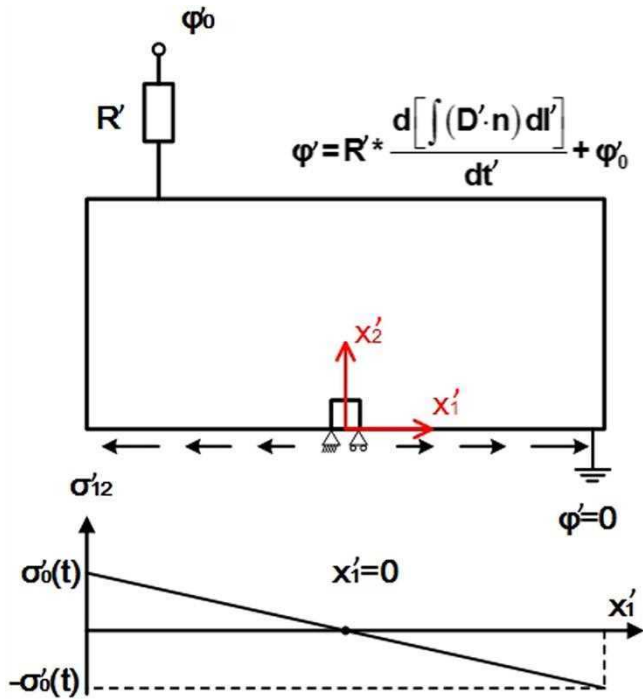


**Figure 4.** Representation of the boundary conditions for the phase field simulation.

as:  $\sigma'_0(t) = \sigma'_0 \sin(\omega t')$ . The normalized time period of the external force taken in the simulation is  $6.4 \times 10^5$ . A fixed electric potential  $\varphi'_0$  is applied on the upper boundary in series with bias resistance  $R'$ , while the lower boundary is electrically grounded. While other electric boundary conditions can be imposed, our main focus in this paper is on this parallel plate case. Simulations with different values of  $\varphi'_0$  and  $R'$  have been conducted to investigate their effects on the energy harvesting capability of the new strategy. The governing equation for the upper electrical boundary condition can be deduced from the conservation law of electrical charge in combination with Ohm's law. 'Zero flux' limitation is imposed for all the other mechanical and electrical boundary conditions. As done by most researchers, natural boundary conditions are adopted for the time-dependent Ginzburg–Landau equation. The initial condition for the polarizations is set as:  $p'_1 = 1$  and  $p'_2 = 0$ , which leads to a convergent simulation. The free Quad meshing method built in the software is employed and the maximum element size in the simulation is kept as 5.

## Results and discussions

### New energy harvesting mechanism demonstration

To demonstrate the energy harvesting mechanism of the proposed strategy and the related nonlinear hysteretic polarization switching phenomenon, a typical energy harvesting process for the parallel plate mode is shown in figure 5. The normalized bias electric potential  $\varphi'_0$  and bias resistance  $R'$  in this simulation are 0.3 and 5 respectively. All the polarizations point in the positive  $x'_1$ -direction ([1 0] phase), when the

simulation starts, which is consistent with the prescribed initial condition. Then the polarization evolves quickly to accommodate the 'zero flux' electric boundary conditions (left and right boundaries) as shown in figure 5(a) (2) at  $t' = 1000$ . As the external compressive stress increases, the domain with polarization in the negative  $x'_2$ -direction ([0  $\bar{1}$ ] phase) grows by the motion of the  $90^\circ$  domain wall as shown in figures 5(a) (3)–(4), until it completely occupies the entire computational area as shown in figure 5(a) (5) at  $t' = 30000$ . In contrast, the domain with polarization in the positive  $x'_2$ -direction ([0 1] phase), which is also stress-favored, does not grow but vanish. This is a direct result of the imposed bias electric potential  $\varphi'_0$ . The domain pattern does not change as the external compressive stress increases to its peaks, then begins to decrease and subsequently turns tensile. When the tensile stress increases to a sufficient level, new domains with horizontal polarizations nucleate at the soft-spot separated from the [0  $\bar{1}$ ] phase by  $90^\circ$  domain wall and begin to grow. Theoretically, both the [1 0] and [ $\bar{1}$  0] phases can be induced from the energy point of view, but it has no effect on the performance of the energy harvesting devices as pointed out above. In the current simulation, both of these two phases are firstly induced as shown in figures 5(a) (8)–(10). However, as calculation continues, the [ $\bar{1}$  0] phase occupies most of the computational area at last as shown in figure 5(a) (11). Only minor changes occur near the left and right boundaries, which seek a maximum volume of the tensile stress-favored polarization, as the external tensile stress increases to its peak as shown in figure 5(a) (12) at  $t' = 4.80 \times 10^5$ . As the tensile stress decreases to zero, the bias electric potential-favored polarization grows slightly as shown in figures 5(a) (13)–(14). The whole process is repeated for subsequent cycles of the external stress.

Figure 5(b) displays the temporal evolutions of average polarization in  $x'_2$ -direction and electric current through the resistance. The external stress curve is added into the figure for reference. In each stress cycle, there exist two abrupt changes in the polarization curve, to which two electric pulses correspond. These two abrupt changes are ascribed to the stress-induced polarization switching via domain nucleation or domain wall motion. Between every two abrupt changes, the polarization alters with the external stress slowly due to the intrinsic stress dependence of the polarization (piezoelectric effect), which is the fundamental mechanism of the traditional piezoelectric energy harvesters. The corresponding electric current is hardly noticeable when compared to that associated with the stress-induced polarization switching process. Thus, the energy density is largely increased with the new strategy, but the electric pulses can be harmful for the energy harvesting circuit, which needs to be carefully studied and handled in the future work. Additionally, the hysteresis loops between the average polarization and external stress are displayed in figure 5(c).

Further, to make a direct comparison between the energy power of the current strategy and that in [16], the electric energy, extracted by the bias resistance in a single period, is

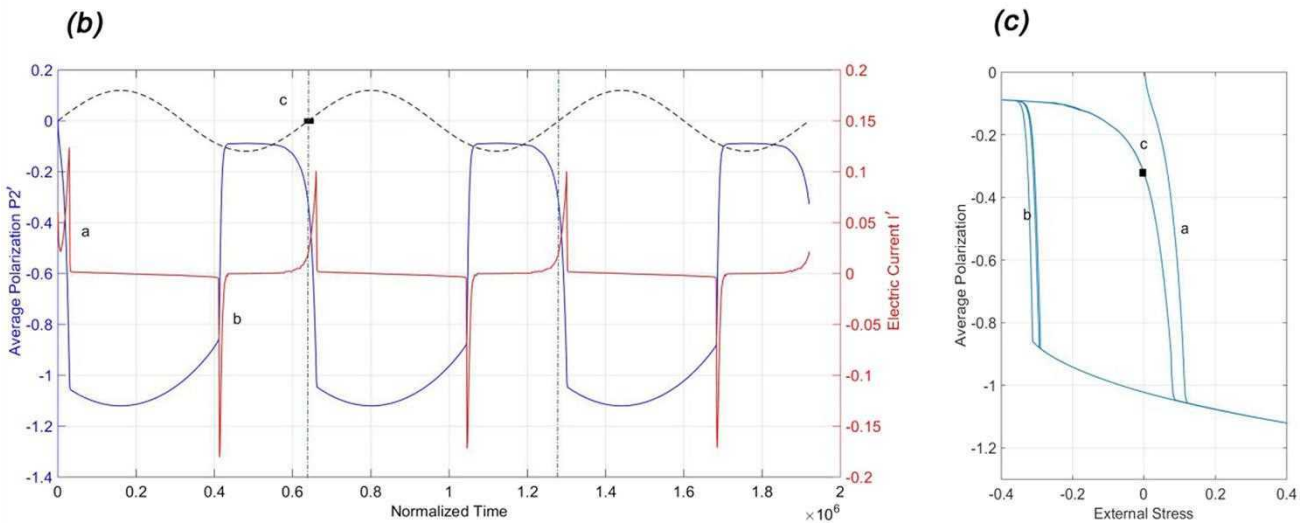
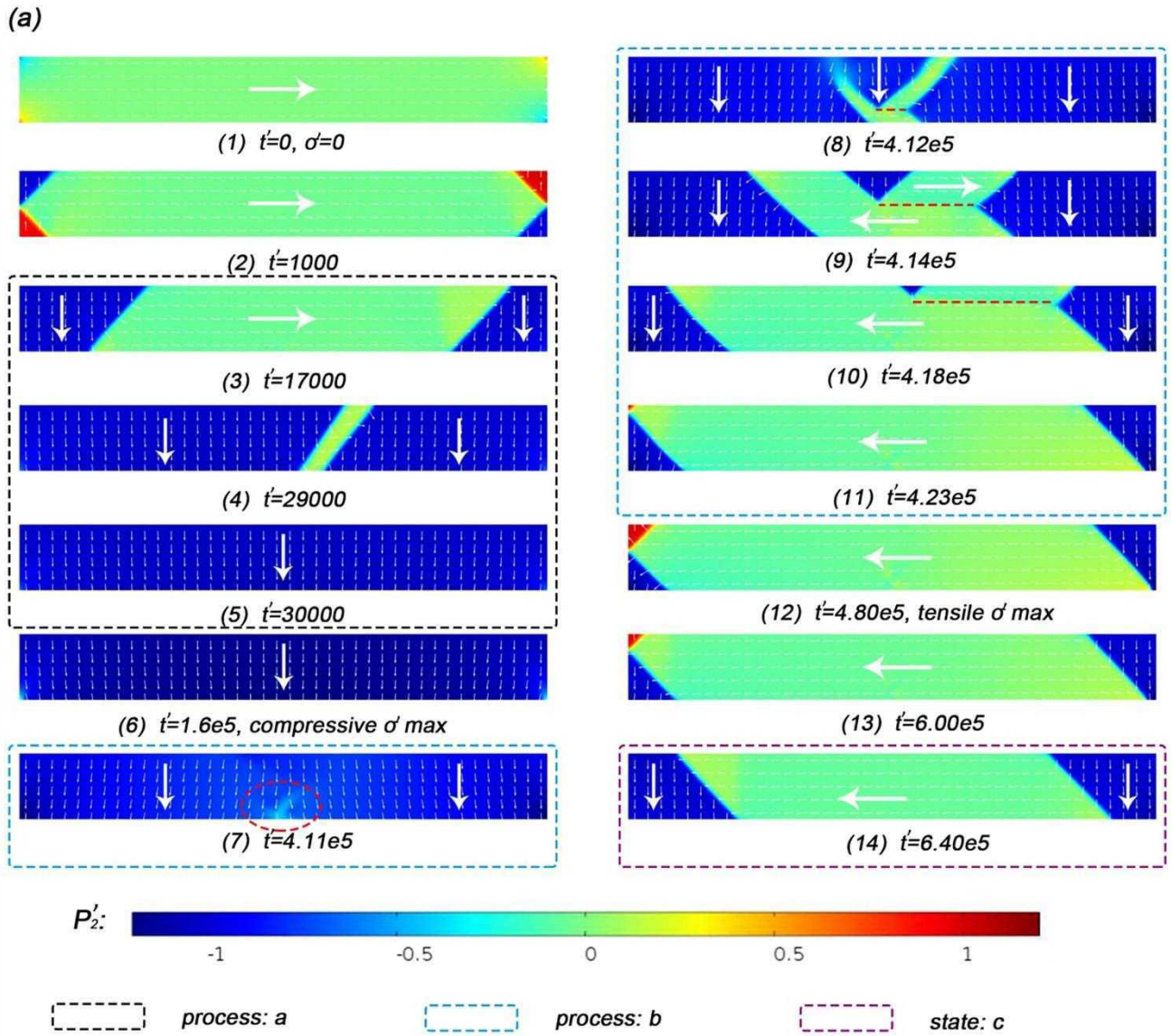


Figure 5. Energy harvesting process with  $\phi'_0 = 0.3$ ,  $R' = 5$ : (a) domain pattern evolution; (b) temporal evolution of average polarization and electric current; (c) hysteresis loop  $P_2'-\sigma'$ .

computed by:

$$\begin{aligned} W'_{\text{output}} &= \oint I'^2 R' dt' = \oint \left( \frac{\varphi' - \varphi'_0}{R'} \right)^2 \\ R' dt' &= \oint \frac{(\varphi' - \varphi'_0)^2}{R'} dt'. \end{aligned} \quad (2)$$

The normalized energy output computed in the current simulation is 1093.94. The corresponding real value equals to  $1093.94 \cdot a_0 p_0^2$ . Thus the energy output per unit area can be deduced as  $1093.94 \cdot a_0 p_0^2 / (l' p_0 \sqrt{a_0/c_0})$ , which equals to  $0.17 \text{ J m}^{-2}$ . It's noticed that the energy harvested here is larger than that in [16] ( $0.04 \text{ J m}^{-2}$ ). This directly results from the larger external stress range imposed here. Instead, the stress range in [16] needs to be carefully designed and has a strict limitation due to the robustness deficiency. The elastic energy input in the current simulation is calculated as 3720.34 by:

$$W'_{\text{input}} = \oint \left( \int_{\text{lower bd.}} \sigma'_{12} \cdot \frac{\partial u'_1}{\partial t'} dx'_1 \right) dt'. \quad (3)$$

Thus the theoretical energy efficiency  $W'_{\text{output}}/W'_{\text{input}}$  is 0.294.

#### Effects of bias resistance $R'$

Simulations with different  $R'$  values have been carried out, which reveal that the bias resistance  $R'$  has a big effect on the nonlinear hysteretic polarization switching process and the quantity of harvested energy. There are two extreme cases, one with  $R' = 0$  and the other with  $R' \rightarrow \infty$ . For the former one, the energy harvesting circuit is shorted and the electric potential on the upper boundary is fixed with the bias one  $\varphi'_0$ . So the polarization switching is induced under a fixed bias electric field ( $-\varphi'_0/h'$ ). However, as  $R'$  equals to 0, no electric energy can be harvested in this condition. For the latter case, the energy harvesting circuit equals to be turned off and the bias potential has no effect. To accommodate the 'zero flux' (no electric current) electric boundary condition for the upper boundary, many small domains are formed, which makes the polarization switching difficult. Thus, the amount of energy harvested in this situation is also very small.

To demonstrate the effect of resistance  $R'$ , an energy harvesting process with a different  $R'$  value ( $\varphi'_0 = 0.3$ ,  $R' = 42$ ) is shown in figure 6. As the external compressive stress increases, in addition to the  $[0 \bar{1}]$  phase, the  $[0 1]$  phase also grows but with a lower speed as shown in figure 6(a) (3), which is different from the situation shown in the above simulation with  $R' = 5$ . With a larger  $R'$  value, it is more difficult for the surface charge accumulated on the upper boundary due to the average polarization change to release. So the speed of average polarization change is slowed down, which is achieved by the growth of the  $[0 1]$  phase. Figure 6(a) (4) shows the exact moment when the horizontal  $[1 0]$  phase disappears and the  $180^\circ$  domain wall between the  $[0 1]$  phase and  $[0 \bar{1}]$  phase forms. With the stress further increasing, the bias electric potential-favored  $[0 \bar{1}]$  phase grows at the cost of  $[0 1]$  phase via the movement of  $180^\circ$  domain wall as shown in figures 6(a)

(5)–(6). The  $[0 \bar{1}]$  phase finally occupies the whole computational area at  $t' = 2.74 \times 10^5$  as shown in figure 6(a) (7). As in the case with  $R' = 5$ , when the tensile stress is sufficiently large, horizontal phases nucleate. Here, only the  $[\bar{1} 0]$  phase is induced, which is different from the situation above but confirms the theoretical prediction.

The corresponding temporal evolution curves of average polarization and electric current are displayed in figure 6(b). The two sharp polarization changes become flatter in the current simulation, especially the first one. The electric pulses in the electric current have also been flattened, and a clear flat current step can even be seen at the place which the first pulse should occupy. The ripple wave associated with the flat current step can be ascribed to the numerical calculation errors. The difference between the first and second electric pulses results from the asymmetry between the two polarization switching processes marked as 'a' and 'b' in the figure. It is reasonable to expect that this difference will be homogenized in polycrystalline materials. Additionally, the hysteresis loop shown in figure 6(c) is much wider when compared to the one with  $R' = 5$  shown in figure 5(c). The associated output energy in a single cycle and energy efficiency in this simulation are  $0.39 \text{ J m}^{-2}$  and 0.575 respectively. Both are improved when compared with the first simulation.

To further demonstrate the  $R'$  effects, stable hysteresis loops between the average polarization and external stress with different  $R'$  values (same potential  $\varphi'_0 = 0.3$ ) are shown in figures 7(a)–(c). In addition, the relationship between the normalized energy harvested in a single stress cycle and the bias resistance  $R'$  is displayed in figure 7(d). From the figures, we notice that the influence of  $R'$  on the energy harvesting behavior can be divided into three regions. When the normalized value of  $R'$  increases from 0 to 30, the energy harvested in each stress cycle increases rapidly. In this region, the compressive stress-induced  $[0 \bar{1}]$  phase can occupy the whole computational area (in other words, polarization switching process 'a' can finish) before the stress reaches its peak. The increasing speed of the energy slows down when  $R'$  is in the region from 42 to 78. In this region, the  $[0 \bar{1}]$  phase cannot occupy the whole area before the compressive peak. However, the process continues after the stress peak with the aid of bias electric potential. This process can be finished before the tensile stress-induced horizontal phases nucleate. When  $R'$  is larger than 78, the energy harvested in each stress cycle decreases with the  $R'$  value increasing. This can be ascribed to the fact that more and more proportions of the polarizations are locked by the larger resistance  $R'$ , which means the related polarization variation is limited.

#### Effects of bias electric potential $\varphi'_0$

Besides the bias resistance, the effects of bias electric potential  $\varphi'_0$  have also been investigated. The polarization switching phenomenon in ferroelectric materials is the result of the competition and transition between electric energy

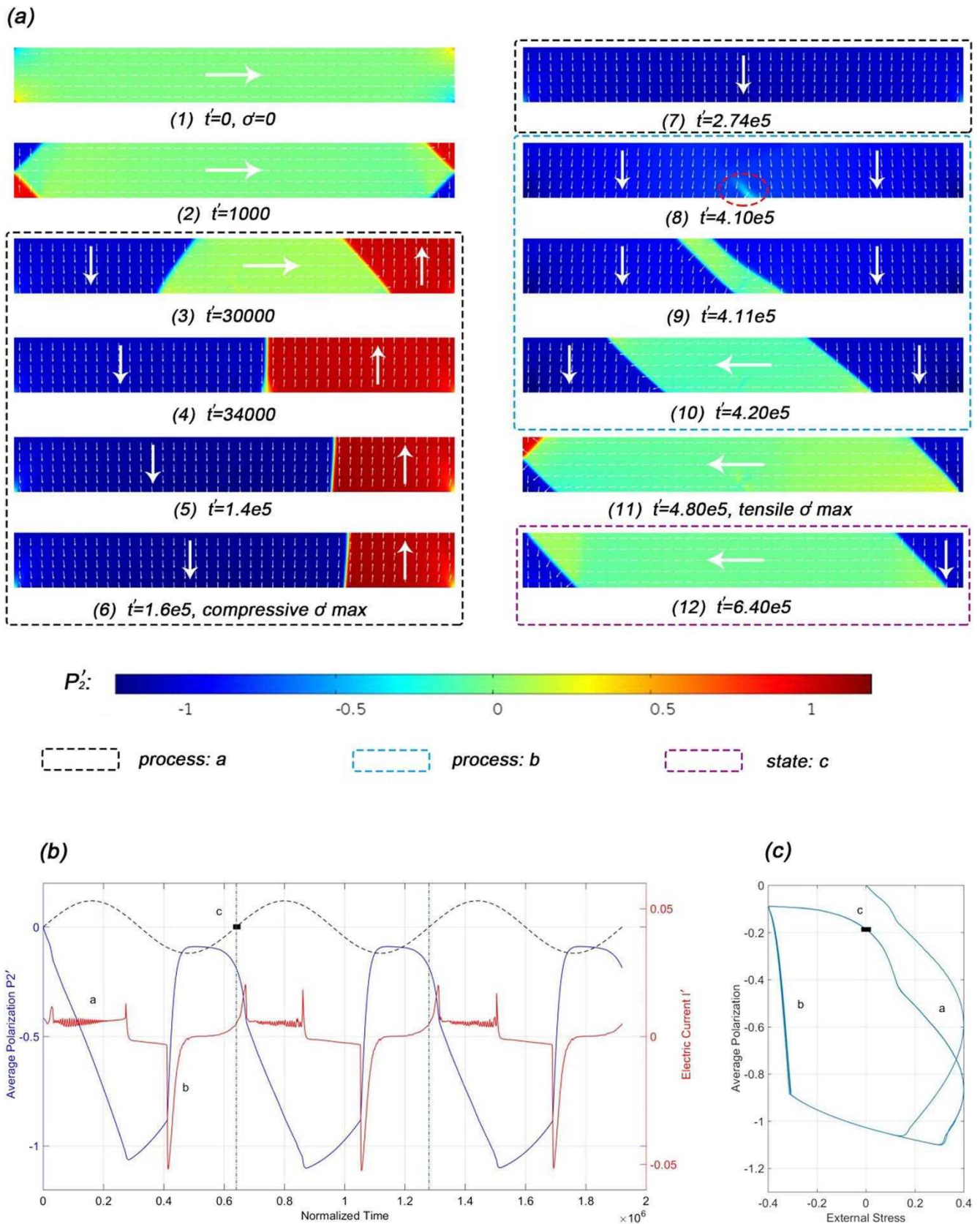


**Figure 6.** Energy harvesting process with  $\varphi'_0 = 0.3, R' = 42$ : (a) domain pattern evolution; (b) temporal evolution of average polarization and electric current; (c) hysteresis loop  $P'-\sigma'$ .

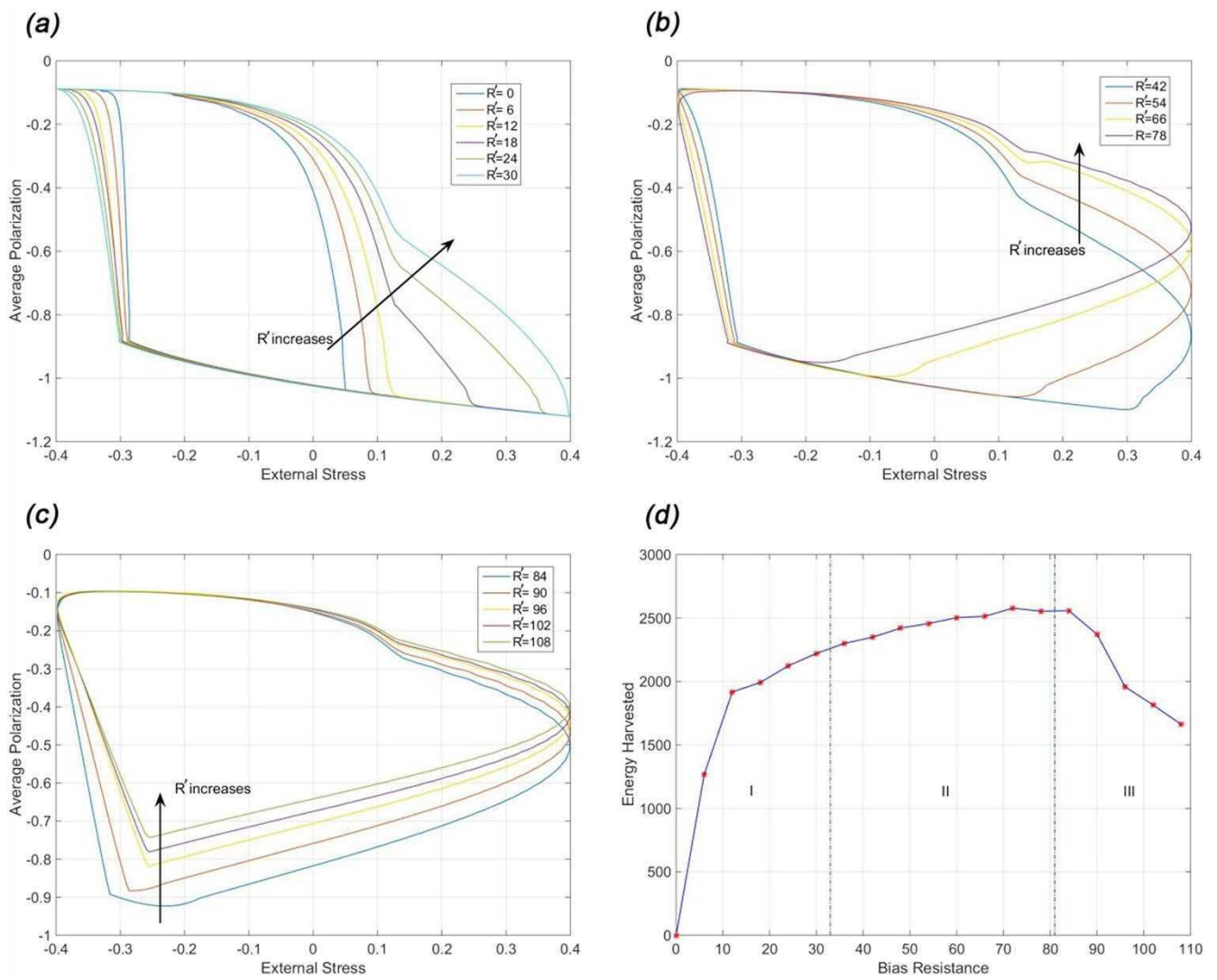


**Figure 7.** Demonstration of the influence of bias resistance  $R'$ : (a) hysteresis loops in region I; (b) hysteresis loops in region II; (c) hysteresis loops in region III; (d) normalized energy curve.

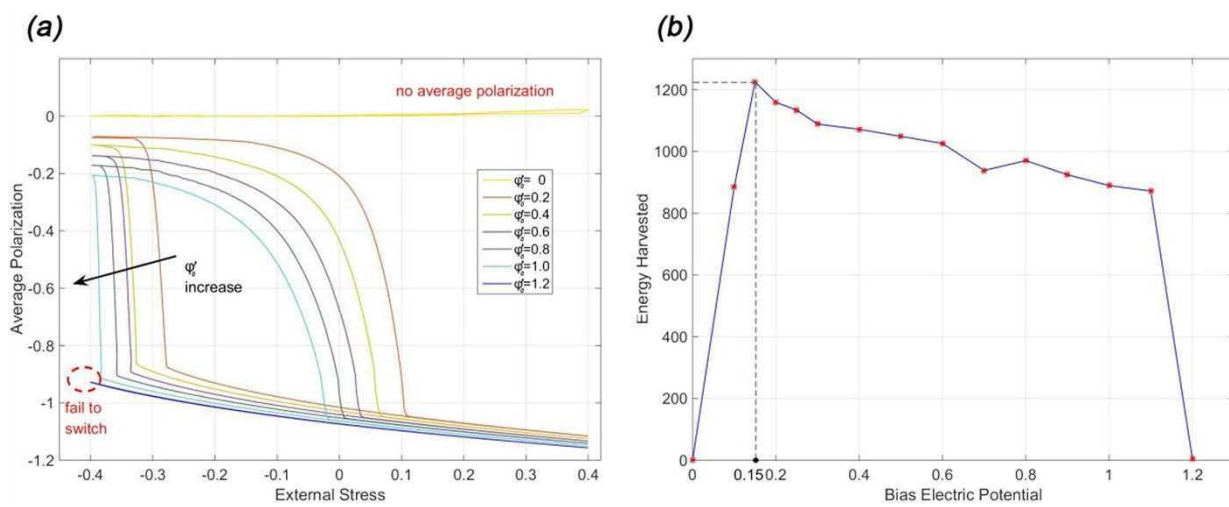


**Figure 8.** Demonstration of the influence of bias electric potential  $\phi_0'$ : (a) hysteresis loops; (b) normalized energy curve.

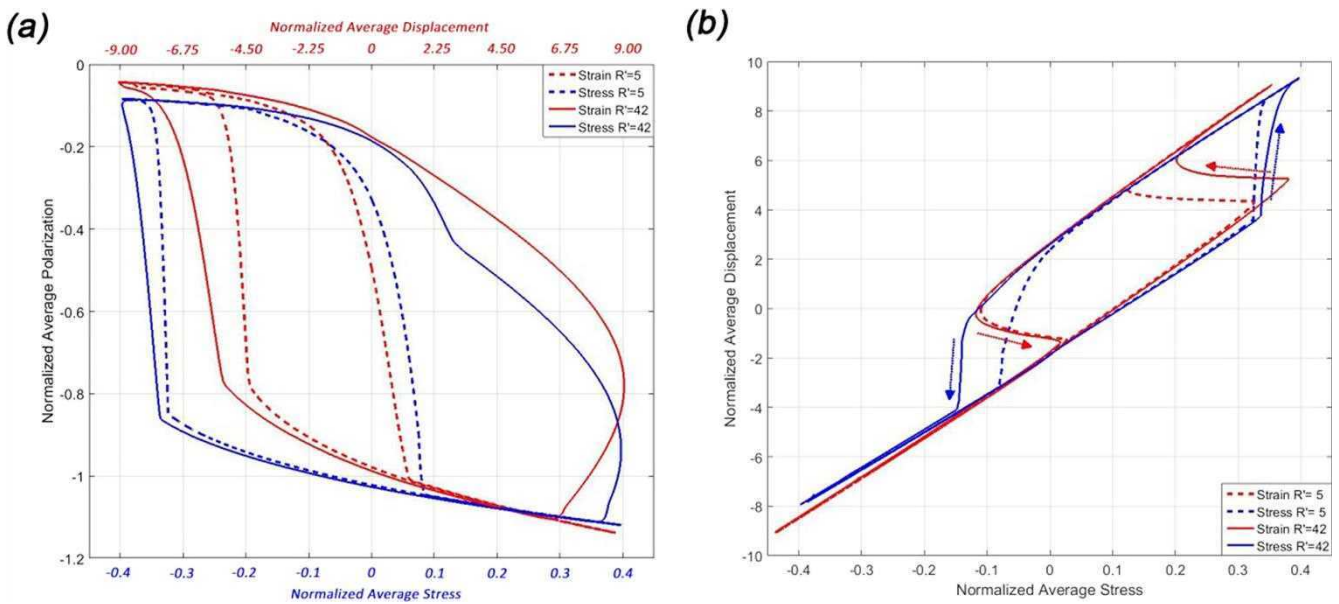


**Figure 9.** Demonstration of effects of mechanical boundary conditions: (a) polarization variations with respect to imposed displacement or stress; (b) displacement–stress relations.

and mechanical energy. As pointed out above, without external bias electric potential, two types of vertical polarization (the  $[0\ 1]$  phase and  $[0\ \bar{1}]$  phase) can be induced with equal chances by the compressive stress. When the prescribed bias electric potential is imposed, a preference is introduced. In addition, the introduced bias electric potential aids the switching from horizontal directions to vertical ones. That is to say, the bias electric potential plays a similar role as the compressive stress. It is reasonable to expect that with a larger bias electric potential, the direct switching (from horizontal directions to vertical ones) becomes easier while the inverse switching more difficult. These theoretical predictions have been proved by the hysteresis loops (with same resistance  $R' = 5$ ) shown in figure 8(a). When the normalized bias electric potential is as large as 1.2, the inverse switching is even prohibited by the bias electric potential. In addition, figure 8(b) displays the corresponding relationship between the normalized energy quantity and bias electric potential.

#### Effects of mechanical boundary conditions

In the above simulations, the mechanical interactions between the ferroelectric thin film and vibrational substrate are captured by imposing a shear stress-type boundary condition, which is different from the strategy adopted in [16] where a uniform strain was applied. To compare the effects of these two boundary conditions, additional simulations with strain-type mechanical boundary condition have been carried out. As in [16], the strain-type boundary condition is implemented by specifying the horizontal displacement  $u_1'(x')$ . The maximum normalized average displacement of the film is kept as 9, which is on the same level as that in the original simulations. The time period is kept identical. The polarization switching processes in these

two types of simulations are quite similar, which can be confirmed by the polarization evolution curves with respect to the imposed displacement or stress, as shown in figure 9(a). In addition, it is noticed that the bias resistance  $R'$  has a similar effect in both cases. The main difference between these two mechanical boundary conditions lies in the stress–displacement relations, as shown in figure 9(b). In simulations with strain-type boundary condition, the displacement is kept nearly constant while the stress has a quite noticeable variation during the polarization switching process. In contrast, the stress is nearly constant while the displacement changes quite visibly in the stress-type case. In the new simulations with strain-type boundary condition, the normalized energy output in a single cycle for parameters  $R' = 5$  and  $\varphi'_0 = 0.3$ , as well as for  $R' = 42$  and  $\varphi'_0 = 0.3$ , are 855.98 and 2180.49, respectively, which are on the same level as the cases with stress-type boundary condition. It needs to be pointed out that both types of the mechanical boundary conditions are only simple approximations of the actions imposed by the deformed substrate. For a more precise simulation, the dynamics of the substrate needs to be taken into consideration, but it would be quite computationally costly. From the literature, stress-type boundary conditions are often used in fluid–structure interactions, which would be the case when acoustic energy harvesting is considered [32]. Even though strain-type boundary conditions are more popular when considering material interfaces in solid mechanics, some examples where the stress-type boundary condition is applied can still be found [33, 34]. Here, the stress-type boundary condition is adopted to demonstrate a new possibility to implement the problem. Considering the quasi-static condition, the differences between the results of these two mechanical

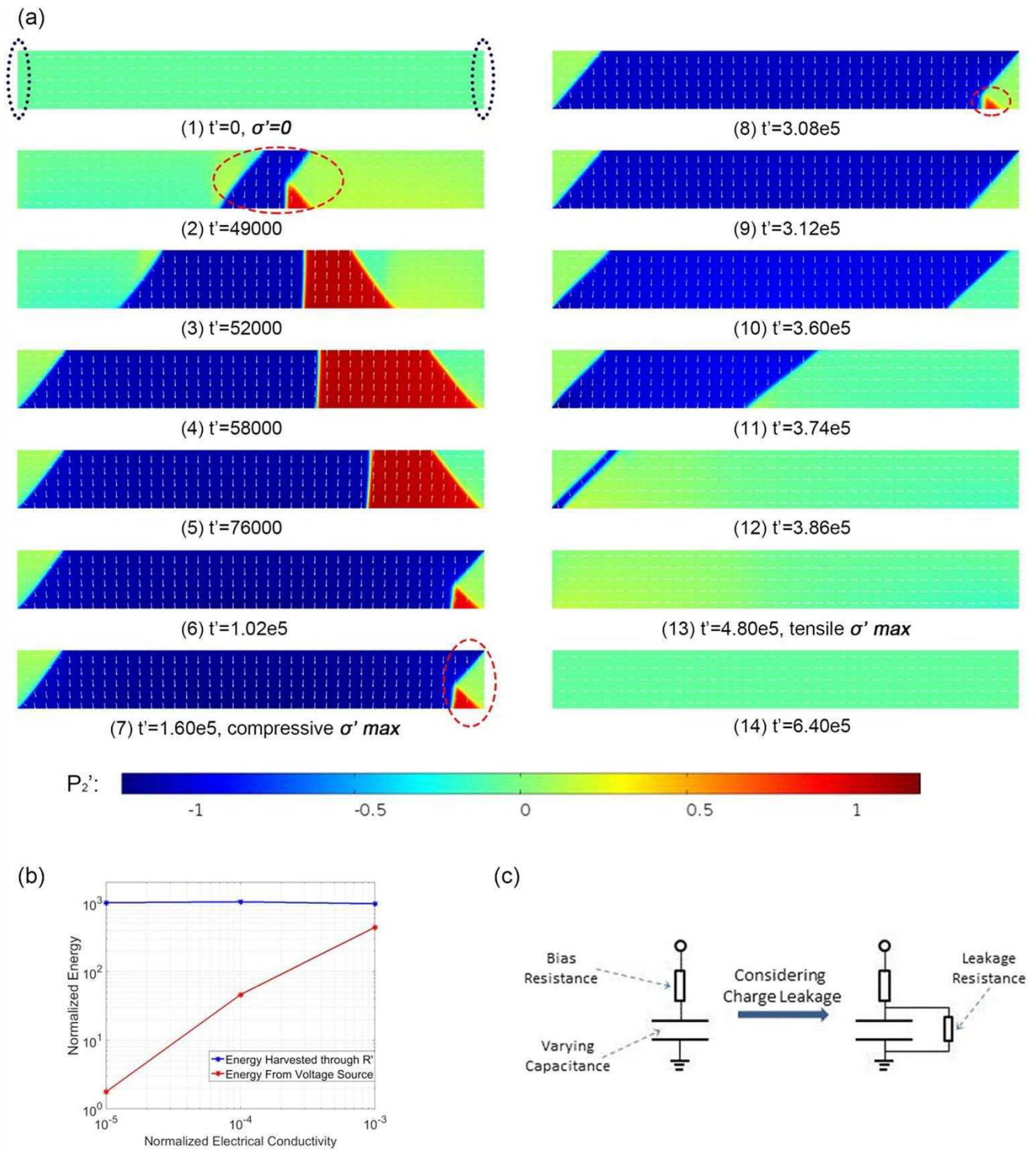


**Figure 10.** Demonstration of charge leakage effect: (a) a typical energy harvesting process including charge leakage effect; (b) energy-electrical conductivity relations; (c) a schematic representation for a simple direct way to study the problem.

boundary conditions are very small, which has been validated by the additional simulations.

*Effects of charge leakage*

Generally, ferroelectric materials are regarded as insulators which have no free charges. However, a vast majority of the

ferroelectrics are actually wide-band-gap semiconductors, which exhibit characteristic properties originating from drift and diffusion of free charges [35–37]. Considering the fact that a relatively high bias electric field is imposed here, the effects of charge leakage or electrical conductivity need to be discussed.

A simple direct way to consider this problem is to separate the effect of charge leakage from the polarization

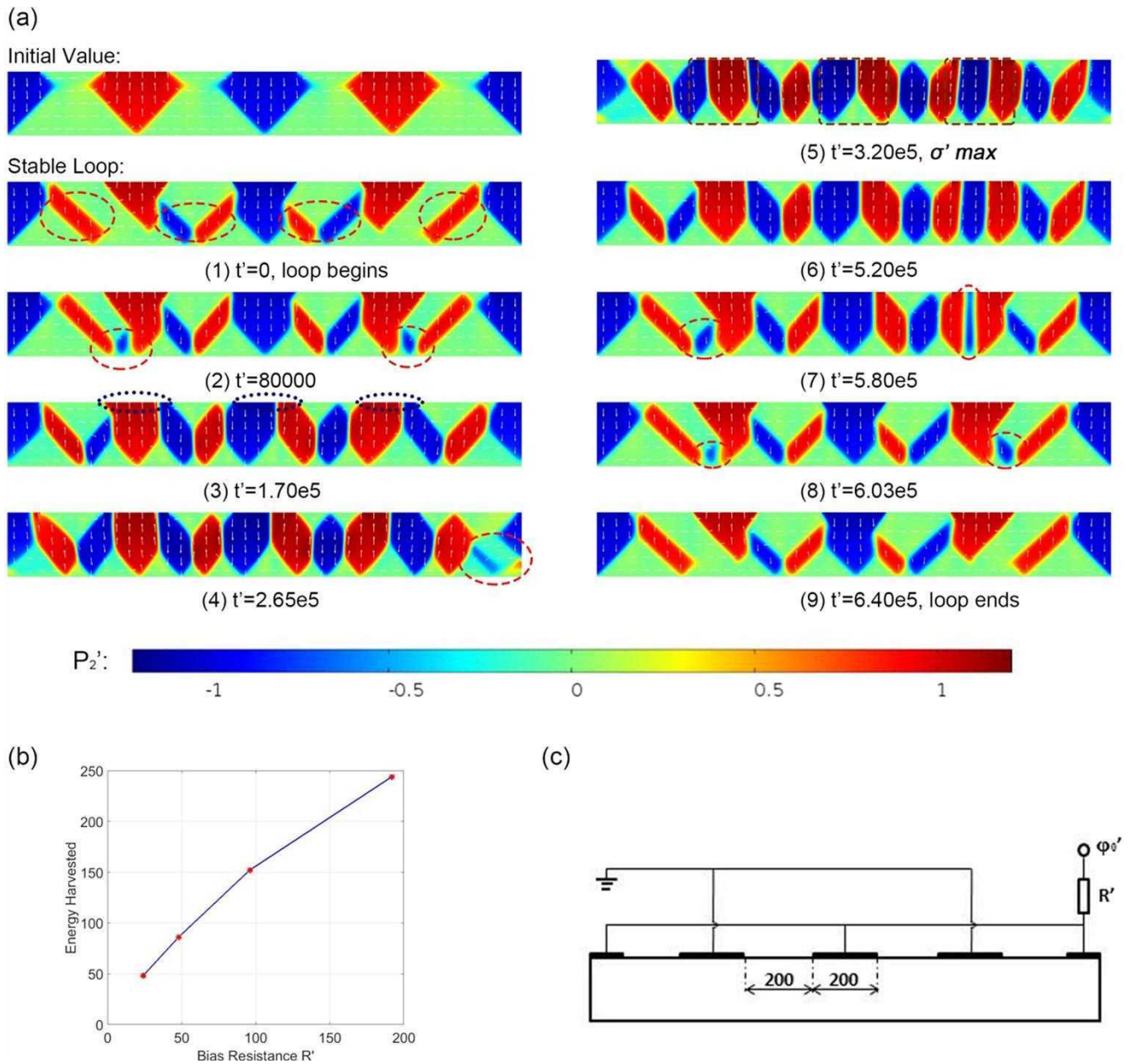


**Figure 11.** Demonstration of interdigitated prototype mechanism: (a) a typical energy harvesting process with interdigitated electrodes arrangement; (b) energy-bias resistance relation; (c) electrical boundary conditions.

switching process and represent it as a leakage resistance, as shown in figure 10(c). However, the polarization switching process and charge leakage process are fully-coupled [35–37]. The polarization switching process in semiconductors is quite different from that in insulators. To investigate the charge leakage effect, several modifications have been implemented in the standard phase-field model for ferroelectrics [37, 38]. For more details, see appendix A.

A typical energy harvesting process, considering charge leakage or electrical conductivity effect, is shown in figure 10(a) ( $\varphi'_0 = 0.3$ ,  $R' = 5$ ,  $\gamma' = 0.0001$ ). Different from the previous simulation in figure 5(a), the normal component of polarizations  $\mathbf{p} \cdot \mathbf{n}$  at both ends of the thin film will not vanish quickly, but will remain during the whole process. This results from the fact that in the current simulation free charges are allowed to exist at

both ends to accommodate the normal component of polarizations  $\mathbf{p} \cdot \mathbf{n}$  at the boundary due to the electrical conductivity. Further, the free charges existing in both ends will lock the nearby polarizations. As the external compressive stress increases, at  $t' = 49\,000$ , new domains with vertical polarizations nucleate, as shown in figure 10(a) (2). Both the  $[0\ 1]$  and  $[0\ \bar{1}]$  phases are induced, but the volume of  $[0\ \bar{1}]$  phase grows at a faster rate due to the existence of bias electric field. At  $t' = 1.02 \times 10^5$ ,  $[0\ \bar{1}]$  phase occupies most of the area and only a small fraction of  $[0\ 1]$  phase exists near the right boundary to accommodate the locked  $[1\ 0]$  phase. The topology of the domain remains the same, as the external compressive stress increases to its peak. As the compressive stress decreases, the mechanical energy near the right boundary is released through domain evolution, as shown in figures 10(a) (8)–(9). Then, the

external stress turns tensile. With the tensile stress increasing to a sufficient level, tensile stress-favored horizontal polarizations start to grow through 90° domain wall motion, as shown in figures 10(a) (10)–(12). Finally, [1 0] phase occupies the entire film and remains the same as the tensile stress increases to its peak and decreases to zero. The entire polarization switching process is quite different from the corresponding process without electrical conductivity, as shown in figure 5(a).

Simulations with different electrical conductivity constants have also been carried out. The normalized energy harvested through the bias resistance  $R'$  and done by the bias voltage source is shown in figure 10(b). The harvested energy through the bias resistance is nearly constant while the energy from the bias voltage is approximately linear with electrical conductivity constant. When the normalized electrical conductivity reaches 0.001, almost half of the energy harvested by the resistance is from the voltage source.

#### *Interdigitated prototype mechanism demonstration*

Finally, to give a basic comparison between the working principles of the prototypes with different electrodes arrangements, the phase-field model has been further modified and implemented to study the interdigitated mechanism. The electrical boundary conditions in these simulations are as shown in figure 11(c). As mentioned above, in this prototype the ferroelectric film is subjected to compressive stress only. The time period of the external stress is kept the same as before. A consistent initial value, as shown in figure 11(a), is taken for the simulation. After two cycles, stable simulation loops are formed, as shown in figure 11(a). At the beginning, when the external stress is zero, the fraction of horizontal polarizations, which is favored by the bias electric field, is at its maximum. It is reasonable to expect that, when the bias electric field is increased to a large enough level, the small fractions of vertical polarizations existing among the horizontal domains will disappear (here the bias potential is 0.6). As the external stress increases, additional domains with vertical polarizations nucleate, as shown in figure 11(a) (2). With the vertical domains growing, the average normal component of polarizations  $\mathbf{p} \cdot \mathbf{n}$  at the electrodes decreases, which means that the amount of free charges at the electrodes decreases. Thus, electric current is induced in the external electric circuits. As the external stress further increases, more additional domains with vertical polarizations nucleate, as shown in figure 11(a) (4). When the external stress increases to its peak, several quasi-vortex structures are formed and the average free charges at the electrodes nearly decrease to zero, as shown in figure 11(a) (5). Subsequently, the stress starts to decrease. Under the influence of bias electrical field, domains with horizontal polarizations grow and some of the vertical domains disappear, as shown in figures 11(a) (6)–(9). In this process, the electrical charges at the electrodes increase to their original states.

In addition, simulations with different bias resistances  $R'$  have also been carried out. Different from the prototype with parallel plate electrodes, the bias resistance  $R'$  has very little impact on the polarization switching process. The energy output is approximately linear with bias resistance in a large resistance

range, as shown in figure 11(b). It needs to be pointed out that the resistance value here needs to be multiplied by 4 when compared to the one in the first prototype, because the area of electrodes here is only 1/4 of that in the first prototype.

## Conclusions

In the current paper, a new strategy for vibration energy harvesting based on stress-induced polarization switching has been proposed and two related prototypes have been demonstrated. Advantages and drawbacks associated with these prototypes have been carefully analyzed and discussed. With the aid of a bias electric field, the robustness deficiency problem associated with the work in [16] has been successfully addressed. In addition, the state-of-the-art real-space phase field model has been implemented to investigate the nonlinear hysteretic polarization switching phenomenon present in the energy harvesting process. The simulation has demonstrated that electric current amplitude associated with the polarization switching process is superior over the one with piezoelectric effect. Finally, the effects of several important factors have also been studied by the finite element simulation. These characteristics show big impacts on the energy quantity harvested by the new strategy, thus must be carefully treated and optimized in future real applications.

## Acknowledgments

This work has been supported by the National Natural Science Foundation of China (Grant No. 51575478 and Grant No. 61571007). DW acknowledges the financial support from Zhejiang University for his visit to Wilfrid Laurier University. RM acknowledges the support from the NSERC and CRC program.

## Appendix A. Model details and normalization

The total potential energy density of a ferroelectric material can be written as

$$\begin{aligned}
 F(\nabla \mathbf{p}, \mathbf{p}, \boldsymbol{\varepsilon}) = & \frac{a_0}{2}(p_{1,1}^2 + p_{1,2}^2 + p_{2,1}^2 + p_{2,2}^2) + \frac{a_1}{2} \\
 & \times (p_1^2 + p_2^2) + \frac{a_2}{4}(p_1^4 + p_2^4) + \frac{a_3}{2}p_1^2 p_2^2 \\
 & + \frac{a_4}{6}(p_1^6 + p_2^6) + \frac{a_5}{4}p_1^4 p_2^4 - \frac{b_1}{2} \\
 & \times (\varepsilon_{11}p_1^2 + \varepsilon_{22}p_2^2) - \frac{b_2}{2}(\varepsilon_{11}p_2^2 + \varepsilon_{22}p_1^2) \\
 & - b_3(\varepsilon_{12} + \varepsilon_{21})p_1p_2 + \frac{c_1}{2}(\varepsilon_{11}^2 + \varepsilon_{22}^2) \\
 & + c_2\varepsilon_{11}\varepsilon_{22} + \frac{c_3}{2}(\varepsilon_{12}^2 + \varepsilon_{21}^2).
 \end{aligned}
 \tag{A.1}$$

Here, the first term is the energy penalty associated with domain walls; the next five terms are Landau-type energy; the following three terms denote electroelastic coupling energy and the last three terms correspond to pure elastic energy.  $a_i$ ,  $b_j$  and  $c_k$  are material-specific parameters.

Based on this energy density, the governing equations of polarization evolution are obtained by the variational

**Table B1.** Original material parameters for BaTiO<sub>3</sub>.

Landau coefficients	Coupling coefficients	Elastic constants <sup>a</sup>	Elastic coefficients
$a_1 = -1.0355 \times 10^8 \text{ Nm}^2 \text{ C}^{-2}$	$b_1 = 2.1127 \times 10^{10} \text{ Nm}^2 \text{ C}^{-2}$	$C_{11} = 211 \text{ GPa}$	$c_1 = 185 \text{ GPa}$
$a_2 = -1.9695 \times 10^9 \text{ Nm}^6 \text{ C}^{-4}$	$b_2 = -2.7367 \times 10^9 \text{ Nm}^2 \text{ C}^{-2}$	$C_{33} = 160 \text{ GPa}$	$c_2 = 111 \text{ GPa}$
$a_3 = 3.9389 \times 10^9 \text{ Nm}^6 \text{ C}^{-4}$	$b_3 = 1.1932 \times 10^{10} \text{ Nm}^2 \text{ C}^{-2}$	$C_{12} = 107 \text{ GPa}$	$c_3 = 74 \text{ GPa}$
$a_4 = 8.4489 \times 10^{10} \text{ Nm}^{10} \text{ C}^{-6}$		$C_{13} = 114 \text{ GPa}$	
$a_5 = 2.3943 \times 10^{14} \text{ Nm}^{14} \text{ C}^{-8}$			

<sup>a</sup> Elastic coefficients used in the current model are related to the elastic constants by  $c_1 = (C_{11} + C_{33})/2$ ,  $c_2 = (C_{12} + C_{13})/2$ ,  $c_3 = c_1 - c_2$ .

**Table B2.** Dimensionless material parameters for BaTiO<sub>3</sub>.

Landau coefficients	Coupling coefficients	Elastic coefficients
$a'_1 = -0.007$ , $a'_2 = -0.009$	$b'_1 = 1.4282$ , $b'_2 = -0.185$	$c'_1 = 185$ , $c'_2 = 111$
$a'_3 = 0.018$ , $a'_4 = 0.0261$	$b'_3 = 0.8066$	$c'_3 = 74$
$a'_5 = 5$		

principle and can be written as:

$$\mu \dot{p}_i = \left( \frac{\partial F}{\partial p_{i,j}} \right)_j - \frac{\partial F}{\partial p_i} - \varphi_{,i}, \quad (\text{A.2})$$

$$p_{i,i} - \varepsilon_0 \varphi_{,ii} = 0, \quad (\text{A.3})$$

$$\left( \frac{\partial F}{\partial \varepsilon_{ij}} \right)_j = 0 \quad (\text{A.4})$$

subject to appropriate boundary conditions, where  $1/\mu > 0$  is the mobility and  $\phi$  is the electric potential, which is related to the electric field by  $\mathbf{E} = -\nabla\phi$ .

For the model which includes the charge leakage or electric conductivity effect, the Gauss's law (A.3) needs to be modified:

$$p_{i,i} - \varepsilon_0 \varphi_{,ii} = q^f, \quad (\text{A.5})$$

and the charge conservation law should be added:

$$\frac{\partial q^f}{\partial t} + J_{i,i} = 0, \quad (\text{A.6})$$

where  $q^f$  and  $J_i$  are the free space charge and electric current density, respectively. The charge current density is given by Ohm's law:

$$J_i = \gamma E_i, \quad (\text{A.7})$$

where  $\gamma$  is the electrical conductivity.

For numerical convenience, the governing equations are normalized. The dimensionless material parameters are defined as:

$$\begin{aligned} \mathbf{x}' &= \mathbf{x} \sqrt{c_0/a_0}/p_0, \quad t' = tc_0/\mu p_0^2, \quad \mathbf{p}' = \mathbf{p}/p_0, \\ \varphi' &= \varphi/\sqrt{a_0 c_0}, \quad \mu' = 1, \quad \varepsilon'_0 = \varepsilon_0 c_0/p_0^2, \quad a'_0 = 1, \\ a'_1 &= a_1 p_0^2/c_0, \quad a'_2 = a_2 p_0^4/c_0, \quad a'_3 = a_3 p_0^4/c_0, \\ a'_4 &= a_4 p_0^6/c_0, \quad a'_5 = a_5 p_0^8/c_0, \quad b'_i = b_i p_0^2/c_0, \\ c'_i &= c_i/c_0, \quad R' = R/\mu, \quad \gamma' = \gamma\mu, \end{aligned} \quad (\text{A.8})$$

where  $i = 1, 2, 3$ ;  $c_0$  is a constant with units of stress, which is chosen to be 1 GPa; and  $p_0$  is the spontaneous polarization of the material.

## Appendix B. Material parameters

BaTiO<sub>3</sub> is chosen for the current numerical simulation. The corresponding spontaneous polarization is  $p_0 = 0.26 \text{ C m}^{-2}$ . Other material parameters are listed in table B1. In addition, the dimensionless parameters are provided in table B2.

## References

- [1] Priya S and Inman D J 2009 *Energy Harvesting Technologies* vol 21 (New York: Springer)
- [2] Kim H S, Kim J H and Kim J 2011 A review of piezoelectric energy harvesting based on vibration *Int. J. Precis. Eng. Manuf.* **12** 1129–41
- [3] Kang M G, Jung W S, Kang C Y and Yoon S J 2016 Recent progress on pzt based piezoelectric energy harvesting technologies *Actuators* **5** 5
- [4] Li H, Tian C and Deng Z D 2014 Energy harvesting from low frequency applications using piezoelectric materials *Appl. Phys. Rev.* **1** 041301
- [5] Dhakar L, Liu H, Tay F E H and Lee C 2013 A new energy harvester design for high power output at low frequencies *Sensors Actuators A* **199** 344–52
- [6] Sharpes N, Abdelkefi A and Priya S 2015 Two-dimensional concentrated-stress low-frequency piezoelectric vibration energy harvesters *Appl. Phys. Lett.* **107** 093901
- [7] Quinn D D, Triplett A L, Bergman L A and Vakakis A F 2011 Comparing linear and essentially nonlinear vibration-based energy harvesting *J. Vib. Acoust.* **133** 011001
- [8] Daqaq M F, Masana R, Erturk A and Quinn D D 2014 On the role of nonlinearities in vibratory energy harvesting: a critical review and discussion *Appl. Mech. Rev.* **66** 040801

- [9] Karami M A and Inman D J 2012 Powering pacemakers from heartbeat vibrations using linear and nonlinear energy harvesters *Appl. Phys. Lett.* **100** 042901
- [10] Ren B *et al* 2010 Piezoelectric energy harvesting using shear mode 0.71pb(mg1/3nb2/3)o3-0.29pbtio3 single crystal cantilever *Appl. Phys. Lett.* **96** 083502
- [11] Yang Z and Zu J 2016 Comparison of PZN-PT, PMN-PT single crystals and PZT ceramic for vibration energy harvesting *Energy Convers. Manage.* **122** 321–9
- [12] Dong W D, Gallagher J A and Lynch C S 2014 Ideal energy harvesting cycle using a phase transformation in ferroelectric crystals *Smart Mater. Struct.* **23** 125026
- [13] Dong W D, Finkel P, Amin A, Cunefare K A and Lynch C S 2014 Energy harvesting using the FER–FEO phase transformation in [011] cut single crystal PIN-PMN-PT *J. Intell. Mater. Syst. Struct.* **25** 1786–99
- [14] Patel S, Chauhan A and Vaish R 2014 A technique for giant mechanical energy harvesting using ferroelectric/antiferroelectric materials *J. Appl. Phys.* **115** 084908
- [15] Patel S, Chauhan A and Vaish R 2014 Analysis of high-field energy harvesting using ferroelectric materials *Energy Technol.* **2** 480–5
- [16] Balakrishna A R and Huber J E 2016 Nanoscale domain patterns and a concept for an energy harvester *Smart Mater. Struct.* **25** 104001
- [17] Chen L Q 2008 Phase-field method of phase transitions/domain structures in ferroelectric thin films: a review *J. Am. Ceram. Soc.* **91** 1835–44
- [18] Van Lich L, Shimada T, Nagano K, Hongjun Y, Wang J, Huang K and Kitamura T 2015 Anomalous toughening in nanoscale ferroelectrics with polarization vortices *Acta Mater.* **88** 147–55
- [19] Balakrishna A R and Huber J E 2015 Scale effects and the formation of polarization vortices in tetragonal ferroelectrics *Appl. Phys. Lett.* **106** 092906
- [20] Bhattacharya K, DeSimone A, Hane K F, James R D and Palmstrøm C J 1999 Tents and tunnels on martensitic films *Mater. Sci. Eng. A* **273** 685–9
- [21] Balakrishna A R, Huber J E and Landis C M 2014 Nano-actuator concepts based on ferroelectric switching *Smart Mater. Struct.* **23** 085016
- [22] Shu Y C and Bhattacharya K 2001 Domain patterns and macroscopic behaviour of ferroelectric materials *Phil. Mag. B* **81** 2021–54
- [23] Burcsu E, Ravichandran G and Bhattacharya K 2004 Large electrostrictive actuation of barium titanate single crystals *J. Mech. Phys. Solids* **52** 823–46
- [24] Saren A, Musiienko D, Smith A R, Tellinen J and Ullakko K 2015 Modeling and design of a vibration energy harvester using the magnetic shape memory effect *Smart Mater. Struct.* **24** 095002
- [25] Chaplya P M and Carman G P 2002 Compression of piezoelectric ceramic at constant electric field: energy absorption through non-180 domain-wall motion *J. Appl. Phys.* **92** 1504–10
- [26] Li L J, Li J Y, Shu Y C, Chen H Z and Yen J H 2008 Magnetoelastic domains and magnetic field-induced strains in ferromagnetic shape memory alloys by phase-field simulation *Appl. Phys. Lett.* **92** 172504
- [27] Cao G, Cao Y, Huang H, Chen L Q and Ma X 2016 Analysis of multi-domain ferroelectric switching in BiFeO<sub>3</sub> thin film using phase-field method *Comput. Mater. Sci.* **115** 208–13
- [28] Zhang W and Bhattacharya K 2005 A computational model of ferroelectric domains: I. Model formulation and domain switching *Acta Mater.* **53** 185–98
- [29] Dayal K and Bhattacharya K 2007 A real-space non-local phase-field model of ferroelectric domain patterns in complex geometries *Acta Mater.* **55** 1907–17
- [30] Su Y and Landis C M 2007 Continuum thermodynamics of ferroelectric domain evolution: theory, finite element implementation, and application to domain wall pinning *J. Mech. Phys. Solids* **55** 280–305
- [31] Wang J and Kamlah M 2009 Three-dimensional finite element modeling of polarization switching in a ferroelectric single domain with an impermeable notch *Smart Mater. Struct.* **18** 104008
- [32] Wang F C and Zhao Y P 2011 Slip boundary conditions based on molecular kinetic theory: the critical shear stress and the energy dissipation at the liquid–solid interface *Soft Matter* **7** 8628–34
- [33] Altenbach H and Becker W (ed) 2014 *Modern Trends in Composite Laminates Mechanics* (vol 448) (Berlin: Springer)
- [34] Herakovich C T 2016 *A Concise Introduction to Elastic Solids: An Overview of the Mechanics of Elastic Materials and Structures* (Berlin: Springer)
- [35] Suryanarayana P and Bhattacharya K 2012 Evolution of polarization and space charges in semiconducting ferroelectrics *J. Appl. Phys.* **111** 034109
- [36] Shenoy V B, Xiao Y and Bhattacharya K 2012 Effect of doping on polarization profiles and switching in semiconducting ferroelectric thin films *J. Appl. Phys.* **111** 084105
- [37] Wang J, Chen Z, Shimada T and Kitamura T 2013 Unusual domain evolution in semiconducting ferroelectrics: a phase field study *Phys. Lett. A* **377** 1643–8
- [38] Schwaab H, Deluca M, Supancic P and Kamlah M 2013 Effect of the electric conductivity on the modeling of the poling process of ferroelectric components *J. Mech. Phys. Solids* **61** 504–16